Estimation of Carbon−Carbon Bond Lengths and Medium-Range Internuclear Distances by Solid-State Nuclear Magnetic Resonance

Marina Carravetta,[†] Mattias Edén,[‡] Ole G. Johannessen,[†] Henrik Luthman,[†] Peter J. E. Verdegem,[§] Johan Lugtenburg,[||] Angelika Sebald,[⊥] and Malcolm H. Levitt*,[†,▽]

Contribution from the Physical Chemistry Division, Stockholm University, S-106 91 Stockholm, Sweden, Weizmann Institute of Science, Department of Chemical Physics, Rehovot 76100, Israel, Department of Nutritional Supplements, Numico Research B.V., 6700 CA Wageningen, The Netherlands, Leiden Institute of Chemistry, Leiden University, 2300 RA Leiden, The Netherlands, Bayerisches Geoinstitut, Universität Bayreuth, D-95440 Bayreuth, Germany, and Chemistry Department, Southampton University, S017 1BJ Southampton, England

Abstract: We describe magic-angle-spinning NMR methods for the accurate determination of internuclear dipole−dipole couplings between homonuclear spins-$^1/_2$ in the solid state. The new sequences use symmetry principles to treat the effect of magic-angle sample-rotation and resonant radio frequency fields. The pulse-sequence symmetries generate selection rules which reduce the interference of undesirable interactions and improve the robustness of the pulse sequences with respect to chemical shift anisotropies. We show that the pulse sequences may be used to estimate distances between ^{13}C spins in organic solids, including bond lengths in systems with large chemical shift anisotropies, such as conjugated systems. For bond-length measurements, the precision of the method is ± 2 pm with a systematic overestimate of the internuclear distance by 3 ± 1 pm. The method is expected to be a useful tool for investigating structural changes in macromolecules.

1. Introduction

Solid-state NMR has become a powerful method for investigating details of molecular structure in large molecular systems. Recoupling schemes[1−15] such as rotational resonance,[13] REDOR,[8] and DRAWS[16,17] allow the estimation of internuclear

* Author for correspondence. E-mail: mhl@physc.su.se. Fax: +46-8-152187.
† Stockholm University.
‡ Weizmann Institute of Science.
§ Numico Research B.V.
|| Leiden University.
⊥ Universität Bayreuth.
▽ Southampton University.

(1) Bennett, A. E.; Griffin, R. G.; Vega, S. *NMR Basic Princ. Prog.* **1994**, *33*, 1.
(2) Lee, Y. K.; Kurur, N. D.; Helmle, M.; Johannessen, O. G.; Nielsen, N. C.; Levitt, M. H. *Chem. Phys. Lett.* **1995**, *242*, 304.
(3) Hohwy, M.; Jakobsen, H. J.; Edén, M.; Levitt, M. H.; Nielsen, N. C. *J. Chem. Phys.* **1998**, *108*, 2686.
(4) Rienstra, C. M.; Hatcher, M. E.; Mueller, L. J.; Sun, B.; Fesik, S. W.; Griffin, R. G. *J. Am. Chem. Soc.* **1998**, *120*, 10602.
(5) Rienstra, C. M. Ph.D. Thesis, Massachusetts Institute of Technology, 1999.
(6) Hohwy, M.; Rientra, C. M.; Jaroniec, C. P.; Griffin, R. G. *J. Chem. Phys.* **1999**, *110*, 7983.
(7) Brinkmann, A.; Edén, M.; Levitt, M. H. *J. Chem. Phys.* **2000**, *112*, 8539.
(8) Gullion, T.; Schaefer, J. *Adv. Magn. Res.* **1989**, *13*, 57.
(9) Gross, J. D.; Costa, P. R.; Griffin, R. G. *J. Chem. Phys.* **1998**, *108*, 7286.
(10) Dusold, S.; Sebald, A. *Ann. Rep. NMR Spectrosc.* **2000**, *41*, 185.
(11) Levitt, M. H.; Oas, T. G.; Griffin, R. G. *Isr. J. Chem.* **1988**, *28*, 271.
(12) Oas, T. G.; Griffin, R. G.; Levitt, M. H. *J. Chem. Phys.* **1988**, *89*, 692.
(13) Levitt, M. H.; Raleigh, D. P.; Creuzet, F.; Griffin, R. G. *J. Chem. Phys.* **1990**, *92*, 6347.
(14) van Rossum, B.-J.; de Groot, C. P.; Ladizhansky, V.; Vega, S.; de Groot, H. J. M. *J. Am. Chem. Soc.* **2000**, *113*, 122.
(15) Verdegem, P. J. E.; Bovee-Geurts, P. H. M.; de Grip, W. J.; Lugtenburg, J.; de Groot, H. J. M. *Biochemistry* **1999**, *38*, 11316.

dipole−dipole couplings in the presence of magic angle spinning,[18] which provides optimal signal strength and resolution. The recoupled dipole−dipole couplings provide molecular structural information, since they depend in a predictable way on internuclear distances. The methods are expected to be particularly important for biomolecular systems such as membrane proteins,[19,20] which are often difficult to crystallize and which are frequently unsuitable for solution NMR because of their molecular size, their insolubility, or their tendency to aggregate. Applications of recoupling have been reported in a variety of systems, including peptide aggregates, proteins, and ligands bound to membrane proteins.[19−23]

So far, the solid-state NMR methodology for determining internuclear distances in homonuclear spin pairs, such as ^{13}C nuclei, has concentrated on the determination of medium-range distances (about 200−600 pm). Medium-range distances are structurally informative, since they are often directly related to the torsional angles around single or double bonds, or are indicative of intramolecular or intermolecular contacts. Nevertheless, the measurement of *short-range* distances would also be useful in some circumstances, since bond lengths are sensitive to electronic structure. For example, $^{13}C−^{13}C$ bond lengths, as determined by diffraction measurements, vary from 120 pm for

(16) Gregory, D. M.; Mitchell, D. J.; Stringer, J. A.; Kiihne, S.; Shiels, J. C.; Callahan, J.; Mehta, M. A.; Drobny, G. P. *Chem. Phys. Lett.* **1995**, *246*, 654.
(17) Mehta, M. A.; Gregory, D. M.; Kiihne, S.; Mitchell, D. J.; Hatcher, M. E.; Shiels, J. C. *Solid State Nucl. Magn. Res.* **1996**, *7*, 211.
(18) Lowe, I. J. *Phys. Rev. Lett.* **1959**, *2*, 285.
(19) Davis, J. H.; Auger, M. *Prog. Nucl. Magn. Res.* **1999**, *35*, 1.
(20) Griffin, R. G. *Nat. Struct. Biol.* **1998**, *5*, 508.
(21) Tycko, R. *Curr. Opin. Chem. Biol.* **2000**, *4*, 500.
(22) Watts, A. *Biochim. Biophys. Acta* **1998**, *1376*, 297.
(23) Feng, X.; Verdegem, P. J. E.; Lee, Y. K.; Sandström, D,; Edén, M.; Bovee-Geurts, P.; de Grip, W. J.; Lugtenburg, J.; de Groot, H. J. M.; Levitt, M. H. *J. Am. Chem. Soc.* **1997**, *119*, 6853.

triple bonds to 160 pm for single bonds. Since the function of a ligand or prosthetic group is often associated with structural changes and electronic rearrangments, the accurate measurement of bond lengths could help elucidate the link between structure and function in many biomolecules. One example is the membrane protein rhodopsin where the absorption of light has been modeled in terms of electronic rearrangements in the retinylidene chromophore.[24-26] For large molecules, even the best crystallographic structures do not provide sufficient resolution to settle such detailed bonding questions.

The dipolar couplings between directly bonded ^{13}C nuclei are relatively large: for example, the through-space dipolar coupling between ^{13}C nuclei separated by one double bond has a magnitude of about 3 kHz. Nevertheless, it is often technically difficult to estimate these couplings accurately by NMR. This is because the most interesting electronic environments for ^{13}C nuclei are often associated with large chemical shift anisotropies (CSAs) of the order of 100 ppm or more. Most solid-state NMR experiments for measuring homonuclear dipolar couplings are sensitive to the magnitude and orientations of the CSA tensors, which are often known only approximately. For this reason, many of the current techniques for estimating distances between ^{13}C spins require an isotopic labeling scheme in which at least one of the coupled spins has a small value of the CSA. In addition, some distance estimation methods, such as rotational resonance,[13] require a large isotropic chemical shift separation of the coupled sites. These restrictions make it difficult to study systems such as unsaturated chains, which usually have closely spaced isotropic shifts and large CSAs.

An additional difficulty of many existing recoupling methods is that they involve the repetitive application of rather long pulse sequences. Such methods suffer from digitization problems when the recoupled dipole-dipole interaction is rather strong, as in the case of directly bonded ^{13}C nuclei. It becomes difficult to digitize the rapid dipolar oscillations using integer multiples of the long rf cycles.

In this contribution, we apply a new range of recoupling pulse sequences to the problem of $^{13}C-^{13}C$ coupling estimation in the presence of large CSA interactions. The new methods are based on the use of symmetry theorems for rotor-synchronized pulse sequences.[2-4,7,27-29] These symmetry theorems make it possible to suppress the most important CSA interference terms. At the same time, the new pulse sequences generate double-quantum (DQ) coherences within the ^{13}C pairs, which allow the signals from these spins to be distinguished from those generated by isolated ^{13}C spins. This is also an important issue in biomolecular NMR, where signals from a doubly ^{13}C-labeled ligand are often obscured by the natural abundance ^{13}C background from the bulk of the molecule.

The pulse sequences are based on rather short repetitive elements, and this makes it possible to digitize the rapid dipolar oscillations comfortably. This allows the accurate measurement of relatively strong dipole-dipole couplings.

We assess the performance of the new pulse sequences by numerical simulations and experiments on a selection of $^{13}C_2$-

labeled model systems with a range of $^{13}C-^{13}C$ bond lengths. We show that the new methods have sufficient accuracy for realistic structural investigations in macromolecular systems. The proposed methods can also be used to estimate medium-range distances. This is demonstrated by experiments on model compounds with $^{13}C-^{13}C$ distances up to 400 pm. The limitations of the new pulse sequences are also discussed.

2. Symmetry-Based Double-Quantum Recoupling Sequences

2.1. Symmetry Principles. The symmetry theory for rotor-synchronized pulse sequences has been given in detail in several places[2-4,6,7,27,28] and will not be repeated here. Nevertheless, a brief summary of the technique is useful for appreciation of the issues involved.

The interactions of the nuclear spins are classified in terms of their rotational properties. In general, a nuclear spin interaction term has the rotational properties of an irreducible spherical tensor operator, with rank l for rotations of the molecular framework ("space rank") and rank λ for rotations of the spin polarizations by applied magnetic fields ("spin rank"). For example, the homonuclear dipole-dipole coupling has ranks $(l, \lambda) = (2, 2)$, the homonuclear isotropic J coupling has ranks $(l, \lambda) = (0, 0)$, the isotropic chemical shift has ranks $(l, \lambda) = (0, 1)$, and the chemical shift anisotropy has rank $(l, \lambda) = (2, 1)$. A spin interaction term is fully specified by the space component index m, which takes values of $-l, -l + 1, ..., l$, and a spin component index μ, which takes values $-\lambda, -\lambda + 1, ..., +\lambda$. In general, a rotating sample exposed to a resonant rf field possesses spin interactions with all possible combinations of (l, m, λ, μ). However, in the case of exact magic-angle spinning (meaning that the sample rotation axis subtends an angle of exactly $\tan^{-1}\sqrt{2}$ with respect to the static magnetic field), the components with $l = 2$ and $m = 0$ vanish. The large number of remaining spin interactions complicates the task of pulse-sequence design in rotating solids.

The behavior of the spins under a pulse sequence is often described to a good approximation using average Hamiltonian theory.[30] The first-order approximation to the average Hamiltonian is denoted $\bar{\mathcal{H}}^{(1)}$ and is equal to the sum of a large number of rotational components $\bar{\mathcal{H}}^{(1)}_{lm\lambda\mu}$. In refs 2-4, 7, 27, 28 it is demonstrated, that for certain classes of pulse sequences, symmetry principles greatly restrict the finite terms $\bar{\mathcal{H}}^{(1)}_{lm\lambda\mu}$ appearing in the average Hamiltonian.

Two broad classes of pulse sequences have been designed. The first class of sequences is denoted CN_n^ν, where N, n, and ν are small integers, called the *symmetry numbers* of the pulse sequence. Sequences of the type CN_n^ν may be constructed using a sequence of N radio frequency (rf) cycles timed so as to span exactly n rotational periods of the sample. The rf phase of each cycle is shifted by $2\pi\nu/N$ radians with respect to the previous one, leading to a stepwise phase incrementation. In ref 27 it is shown that CN_n^ν symmetry imposes the following *selection rule* on the first-order average Hamiltonian:

$$\overline{\mathcal{H}}^{(1)}_{lm\lambda\mu} = 0 \quad \text{if } mn - \mu\nu \neq NZ \tag{1}$$

where Z is any integer. For example, the symmetry numbers N, n, and ν may be chosen so that all terms of the form $(l, m, \lambda, \mu) = (2, m, 1, \mu)$ and $(0, 0, 1, \mu)$ are symmetry-forbidden

(24) Shichida, Y.; Ono, T.; Yoshizawa, T.; Matsumoto, H. *Biochemistry* **1987**, *26*, 4422.
(25) Verhoeven, M. A.; Creemers, A. F. L.; Bovee-Geurts, P. H. M.; de Grip, W. J.; Lugtenburg, J.; de Groot, H. J. M. *Biochemistry* **2001**, *40*, 3282.
(26) Mathies, R. A.; Lugtenburg, J. The Primary Photoreaction of Rhodopsin. In *The Handbook of Biological Physics*; Elsevier Science: Amsterdam, 2000; Chapter 2, pp 55-90.
(27) Edén, M.; Levitt, M. H. *J. Chem. Phys.* **1999**, *111*, 1511.
(28) Carravetta, M.; Edén, M.; Brinkmann, A.; Zhao, X.; Levitt, M. H. *Chem. Phys. Lett.* **2000**, *321*, 205.

(29) Brinkmann, A.; Levitt, M. H. *J. Chem. Phys.* **2001**, *115*, 357.
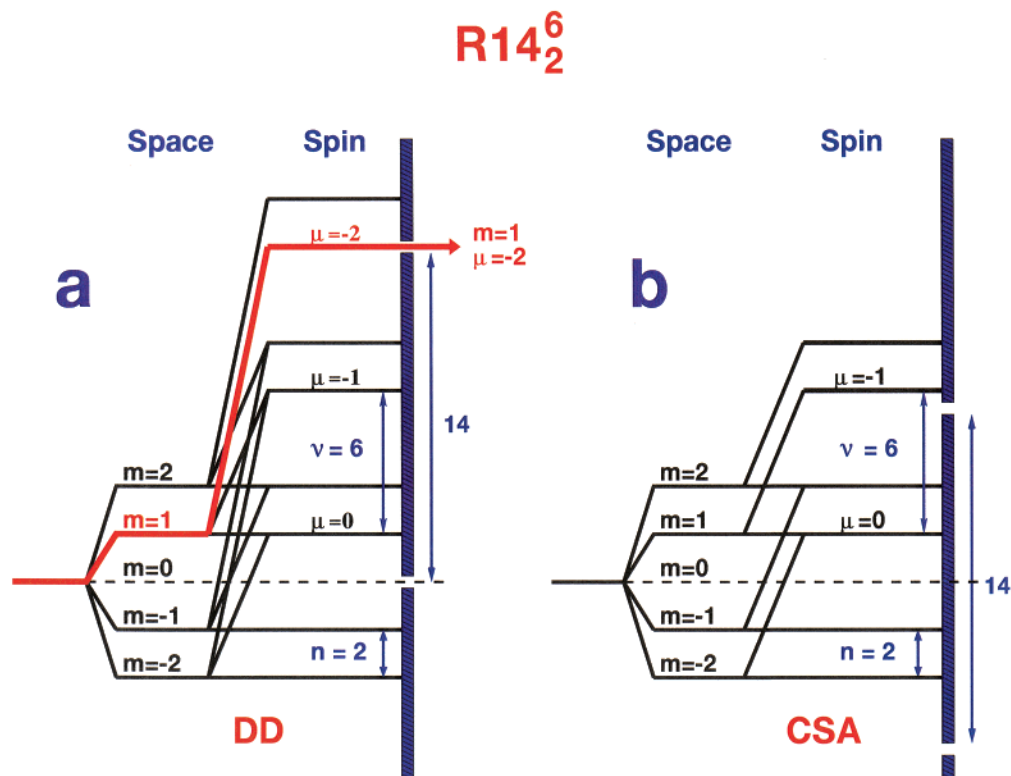(30) Haeberlen, U.; Waugh, J. S. *Phys. Rev.* **1968**, *175*, 453.

$$\text{R14}_2^6$$

Figure 1. Space−spin selection diagram for R14$_2^6$. Terms $\bar{\mathcal{H}}_{lm\lambda\mu}^{(1)}$ are indicated by branching pathways. The vertical wall on the right-hand side of the diagrams represents the first-order selection rule. Pathways with $m < 0$ and $\mu < 0$ have been omitted for simplicity. (a) SSS diagram for the homonuclear dipole−dipole coupling $(l, \lambda) = (2, 2)$. (b) SSS diagram for the chemical shift anisotropy $(l, \lambda) = (2, 1)$.

while two terms of the form $(l, m, \lambda, \mu) = (2, m', 2, 2)$ and $(2, m', 2, -2)$ are symmetry-allowed, where m' is one of $\{-2, -1, 1, 2\}$. All other components of the homonuclear dipole−dipole interaction are suppressed. These solutions implement CSA-compensated homonuclear DQ recoupling with so-called "γ-encoding"[31] of the double-quantum average Hamiltonian. The latter property ensures good performance in a nonoriented sample, such as a powder. Examples include C7$_2^1$ [2−4] and C14$_4^5$.[7] Other solutions are listed in ref 7.

More recently, we have described a second broad class of pulse sequences denoted RN_n^ν.[28] These sequences are based on an element denoted R, which implements a rotation of the resonant spins through the angle π about the rotating-frame x-axis. A second element, denoted R′, is derived from R by reversing the sign of all rf phases (this has no effect if R contains only phase shifts in multiples of π). The RN_n^ν sequence consists of $N/2$ contiguous pairs of elements R$_{\phi_0}$R′$_{\phi_0}$, where ideally the phase shift ϕ_0 is set to the exact value $\pi\nu/N$, although slight adjustments are sometimes made (see section 2.5 below). The RN_n^ν sequence of $N/2$ contiguous RR′ pairs is timed so as to span exactly n rotational periods of the sample. The theory described in refs 29 shows that RN_n^ν symmetry imposes the following selection rule on the first-order average Hamiltonian:

$$\overline{\mathcal{H}}_{lm\lambda\mu}^{(1)} = 0 \quad \text{if } mn - \mu\nu \neq \frac{N}{2}Z_\lambda \tag{2}$$

Here Z_λ indicates an integer of the same parity as that of the spin rank λ; if λ is even, then Z_λ takes the values $Z_\lambda = 0, \pm2, \pm4, ...;$ if Z_λ is odd, then Z_λ takes the values $Z_\lambda = 1, \pm3, \pm5, ...$

The selection rule for RN_n^ν sequences (eq 2) is similar to that for CN_n^ν sequences (eq 1) and admits several solutions for γ-encoded homonuclear DQ recoupling with suppression of CSA terms. Figure 1 shows a space−spin selection diagram (SSS diagram)[29] depicting the first-order selection rules for the case of R14$_2^6$.[28] All possible terms $\bar{\mathcal{H}}_{lm\lambda\mu}^{(1)}$ are indicated by branching pathways. The sum $mn - \mu\nu$ for a given term is indicated by the final vertical level. The vertical wall on the right-hand side of the diagrams depicts the inequality of eq 2. The holes in the wall indicate values of $mn - \mu\nu$ which do not satisfy the inequality and which are symmetry-allowed. In Figure 1a the position of the holes corresponds to the selection rule for even λ, as is in the case of dipole−dipole interactions. In Figure 1b, the position of the holes is appropriate for odd λ, as in the case of chemical shift interactions. The symmetry R14$_2^6$ forbids all first-order average Hamiltonian terms of the form $(l, m, \lambda, \mu) = (2, m, 1, \mu)$ and $(0, m, 1, \mu)$ while admitting the double-quantum dipolar terms $(2, -1, 2, 2)$ and $(2, 1, 2, -2)$. All other homonuclear dipole−dipole terms are suppressed. These properties lead to γ-encoded CSA-compensated DQ recoupling.

There are many other sequences with symmetry properties suitable for achieving CSA-compensated DQ dipolar recoupling. A selection of RN_n^ν symmetries in the range $n \leq 8$, $N \leq 30$ is listed in Table 1. A total of 52 sequences have been found in this range. For all the sequences in Table 1, the terms $(l, m, \lambda, \mu) = (2, -1, 2, 2)$ and $(2, 1, 2, -2)$ are symmetry-allowed. The first-order average Hamiltonian has the form:

$$\bar{\mathcal{H}}^{(1)} = \sum_{j<k}(\omega_{jk}T_{2-2}^{jk} + \omega_{jk}^*T_{22}^{jk}) \tag{3}$$

where $T_{2\pm2}^{jk}$ are second-rank spin operators for the interaction

(31) Nielsen, N. C.; Bildsøe, H.; Jakobsen, H. J.; Levitt, M. H. *J. Chem. Phys.* **1994**, *101*, 1805.

Table 1. RN_n^ν Symmetry Solutions for CSA-compensated, γ-encoded Homonuclear DQ Dipolar Recoupling with $n \leq 8$ and $N \leq 30^a$

Sequence	$R = 90_0\,270_{180}$		$R = 180_0$	
RN_n^ν	ω_{nut}/ω_r	$|\kappa_{2-122}|$	ω_{nut}/ω_r	$|\kappa_{2-122}|$
$R12_2^{-1}$, $R12_2^5$	6	0.170	3	0.174
$R14_2^{-1}$, $R14_2^6$	7	0.172	3.5	0.175
$R16_2^{-1}$, $R16_2^7$	8	0.173	4	0.175
$R18_2^{-1}$, $R18_2^8$	9	0.174	4.5	0.175
$R20_2^{-1}$, $R20_2^9$	10	0.174	5	0.176
$R22_2^{-1}$, $R22_2^{10}$	11	0.175	5.5	0.176
$R24_2^{-1}$, $R24_2^{11}$	12	0.175	6	0.176
$R26_2^{-1}$, $R26_2^{12}$	13	0.175	6.5	0.176
$R28_2^{-1}$, $R28_2^{13}$	14	0.176	7	0.176
$R30_2^{-1}$, $R30_2^{14}$	15	0.176	7.5	0.176
$R14_4^{-2}$, $R14_4^5$	3.5	0.157	1.75	0.168
$R18_4^{-2}$, $R18_4^7$	4.5	0.165	2.25	0.171
$R22_4^{-2}$, $R22_4^9$	5.5	0.169	2.75	0.173
$R26_4^{-2}$, $R26_4^{11}$	6.5	0.171	3.25	0.174
$R30_4^{-2}$, $R30_4^{13}$	7.5	0.172	3.75	0.175
$R14_6^{-3}$, $R14_6^4$	2.3	0.134	1.15	0.157
$R16_6^{-3}$, $R16_6^5$	2.7	0.144	1.3	0.161
$R20_6^{-3}$, $R20_6^7$	3.3	0.155	1.7	0.167
$R22_6^{-3}$, $R22_6^8$	3.7	0.159	1.8	0.168
$R26_6^{-3}$, $R26_6^{10}$	4.3	0.164	2.17	0.171
$R28_6^{-3}$, $R28_6^{11}$	4.7	0.166	2.3	0.172
$R14_8^{-3}$, $R14_8^4$	1.75	0.104	0.88	0.143
$R18_8^{-4}$, $R14_8^5$	2.25	0.104	1.13	0.143
$R22_8^{-4}$, $R22_8^7$	2.75	0.146	1.38	0.162
$R26_8^{-4}$, $R26_8^9$	3.25	0.154	1.63	0.166
$R30_8^{-4}$, $R30_8^{11}$	3.75	0.160	1.88	0.169

^{a} The ratio of the nutation frequency to the spinning frequency is specified for two choices of R elements. All symmetries generate selection rules allowing the terms $(l, m, \lambda, \mu) = (2, -1, 2, 2)$ and $(2, 1, 2, -2)$ and suppressing all other dipole−dipole couplings and chemical shift terms in the first-order average Hamiltonian. Sequences which allow $(l, m, \lambda, \mu) = (2, 1, 2, 2)$ and $(2, -1, 2, -2)$ may be generated by reversing the sign of ν.

between spins j and k. The recoupled interaction between spins j and k is given by refs 2, 3, and 7.

$$\omega_{jk} = \sqrt{6}\,b_{jk}\kappa_{2-122}D_{0-1}^2(\Omega_{PR}^{jk})\,e^{i(\alpha_{RL}^0 + \omega_r t^0)} \qquad (4)$$

where

$$b_{jk} = -(\mu_0/4\pi)\gamma^2\hbar/r_{jk}^3 \qquad (5)$$

is the magnetic dipole−dipole coupling constant, $\Omega_{PR}^{jk} = \{\alpha_{PR}^{jk}, \beta_{PR}^{jk}, \gamma_{PR}^{jk}\}$ is the set of Euler angles relating the principal axis system of the coupling between spins j and k to a rotor-fixed frame, α_{RL}^0 is the initial phase of the rotor, ω_r is the spinning angular frequency, t^0 is the initial time-point of the pulse sequence (defined such that $t = 0$ is the start of data acquisition), and r_{jk} is the internuclear distance. κ_{2-122} is the scaling factor for the pulse sequence and depends on the symmetry numbers and on the element R. Explicit formulas for κ_{2-122} are given in ref 7. Some numerical values of $|\kappa_{2-122}|$ are given in Table 1.

Although symmetries such as $C7_2^1$ and $R14_2^6$ generate equivalent selection rules in the first-order average Hamiltonian, they are inequivalent when higher-order average Hamiltonian terms $\bar{\mathscr{H}}^{(2)}$, $\bar{\mathscr{H}}^{(3)}$, ... are considered. As shown in ref 27, the symmetry theory allows an estimate to be made of the number of symmetry-allowed higher-order terms, which may be taken as a qualitative indicator of the pulse-sequence performance.
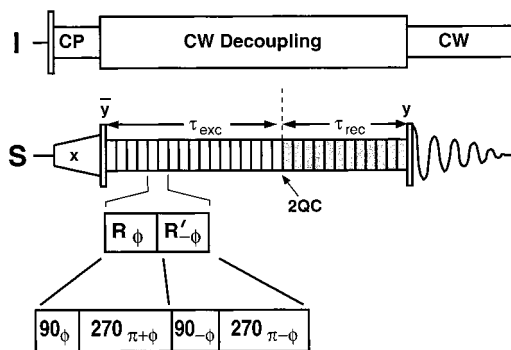

Figure 2. Pulse sequence for $^{13}C-^{13}C$ distance measurements in organic solids. Rf fields at the ^1H Larmor frequency are denoted "I". Rf fields at the ^{13}C Larmor frequency are denoted "S". Ramped cross-polarization followed by a 90° pulse gives enhanced longitudinal ^{13}C magnetization. This is followed by an interval of DQ excitation of duration τ_{exc}. The DQ coherence is then reconverted back to longitudinal magnetization by a sequence of duration τ_{rec} and converted into observable signal by a 90° pulse. The shaded elements are phase-cycled to select signals passing through $\pm 2Q$ coherences. The rotor-synchronized sequence is made up by a repetition of the element $R_{\phi_0}R'_{-\phi_0}$.

In the case of $C7_2^1$ symmetry, there are 54 symmetry-allowed $\bar{\mathscr{H}}^{(2)}$ terms involving commutators of the CSA and the dipole−dipole interactions. In the case of $R14_2^6$, there are only 16 terms of this kind. This qualitative distinction translates into an improved robustness of the $R14_2^6$-based sequences with respect to CSA interactions. This qualitative conclusion is supported by simulations given below.

In practice, the element $R = (\pi/2)_0(3\pi/2)_\pi$ gives favorable performance for many RN_n^ν symmetries. The standard pulse sequence notation β_ϕ is used here: $\beta = \omega_{nut}\tau_p$ is the pulse flip angle, where ω_{nut} is the nutation frequency, τ_p, the pulse duration, and ϕ is the pulse phase. The scaling factors and rf-field requirements of several sequences are listed in Table 1.

In the experiments shown below, we concentrate on applications of the $R14_2^6$ and $R22_4^9$ sequences with $R = (\pi/2)_0(3\pi/2)_\pi$. Explicitly, the $R14_2^6$ sequence is given by

$$R14_2^6 = \{90_{77.1}270_{257.1}90_{282.9}270_{102.9}\}^7 \qquad (6)$$

using degrees for flip angles and phases. The superscript 7 on the right-hand side indicates 7 repetitions of the bracketed elements, spanning a total of 2 rotational periods. The $R22_4^9$ sequence is given by

$$R22_4^9 = \{90_{73.6}270_{253.6}90_{286.4}270_{106.4}\}^{11} \qquad (7)$$

where 11 repetitions of the bracketed sequence span exactly 4 rotational periods.

Other choices of symmetries and basic elements may also be considered. For example, the symmetry $R12_2^5$ using the basic element $R^0 = (\pi/3)_0(5\pi/3)_\pi(\pi/3)_0$ provides good DQ efficiency in simulations. However, thus far it has not performed well in practice, for unclear reasons.

2.2. Pulse Sequences. The pulse sequence used for $^{13}C-^{13}C$ distance measurements in $^{13}C_2$-labeled organic solids is shown in Figure 2. The channel marked "I" indicates irradiation of the ^1H resonance frequency. The channel marked "S" indicates irradiation at the ^{13}C resonance frequency. The pulse sequence involves ramped cross-polarization[32] from the ^1H spins to the ^{13}C spins, followed by a $(\pi/2)_{\bar{y}}$ pulse on the ^{13}C spins to generate

enhanced z-magnetization. A RN_n^ν sequence of duration τ_{exc} converts the spin-pair magnetization into double-quantum coherence. The DQ coherence is reconverted into longitudinal magnetization by a second RN_n^ν sequence of duration τ_{rec}. The longitudinal magnetization is converted into observable transverse magnetization by a $\pi/2$ read pulse. The reconversion interval and read pulse are subject to a standard four-step phase cycle[33] to select NMR signals passing through (± 2)-quantum coherence. In a powder, the theoretical maximum DQ-filtering efficiency for γ-encoded sequences is 73%.[2]

The dipole−dipole coupling between the ^{13}C spins may be estimated by recording a so-called double-quantum build-up curve. This is done by performing several experiments in which the durations of one or both R-sequence blocks are incremented. It is not necessary to restrict the number of elements to integer multiples of N nor to have excitation and reconversion intervals of equal length. We have compared two different procedures for recording build-up curves. In the *symmetric procedure*, the excitation interval τ_{exc} and the reconversion interval τ_{rec} are incremented at the same time, keeping $\tau_{exc} = \tau_{rec}$. This procedure was used in previous applications of DQ recoupling.[2] It produces a build-up curve of the form $\langle \sin^2(|\omega_{jk}|\tau_{exc})\rangle$, where $\langle ...\rangle$ denotes a powder average. In the *asymmetric procedure*, either τ_{exc} or τ_{rec} is fixed at a value corresponding to maximum DQ transfer, and the other interval is changed. The asymmetric procedure produces a curve of the form $\langle \sin(|\omega_{jk}|\tau_{exc}) \sin(|\omega_{jk}|\tau_{rec})\rangle$. The oscillation frequency in the asymmetric procedure is therefore about half of the oscillation frequency in the symmetric procedure. However, the oscillation amplitude is about twice as much for the asymmetric procedure compared to that for the symmetric procedure. Normally, we find the asymmetric procedure to be superior, mainly due to its enhanced dynamic range.

Experimental results for the two procedures are compared for the case of [2,3-^{13}C$_2$]-L-alanine in Figure 3. The plots also show best-fit numerical simulations, using the known CSA orientations for the two sites[34] and a crude relaxation model (see below). In a, the symmetric procedure was used, with both τ_{exc} and τ_{rec} incremented at the same time, keeping $\tau_{exc} = \tau_{rec}$. In b, τ_{rec} was fixed to the optimal value $\tau_{rec} = 523.8$ μs, while τ_{exc} was incremented from 0 to 3.57 ms in steps of 95.2 μs, corresponding to increasing the number of RR′ pairs. The curve in b has slower oscillations but much larger dynamic range. The estimated value of the dipole−dipole coupling constant from the fit was $b_{jk}/2\pi = -2095 \pm 37$ Hz in a and -2105 ± 37 Hz in b. If molecular motion[35] and J anisotropy are neglected, these results correspond to internuclear distances of 153.7 ± 0.9 pm in (a) and 153.4 ± 0.9 pm in (b). Both results are close to the X-ray distance estimate of 152.3 pm.[36]

Note the fine digitization of the build-up curves in Figure 3. This is possible because the R14$_2^6$ sequence has a short basic element, corresponding to a single R element. Although the average Hamiltonian theory used to calculate eq 2 is strictly valid only for complete RN_n^ν cycles, the smooth curves in Figure 3 show that the results are also approximately valid for partial RN_n^ν sequences, too. Many competing methods, such as MELODRAMA[37] and DRAWS,[16] require the completion of

(32) Metz, G.; Wu, X.; Smith, S. O. *J. Magn. Res. A* **1994**, *110*, 219.
(33) Ernst, R. R.; Bodenhausen, G.; Wokaun, A. *Principles of Nuclear Magnetic Resonance in One and Two Dimensions*; Clarendon Press: Oxford, 1988.
(34) Naito, A.; Ganapathy, S.; Akasaka, K.; McDowell, C. A. *J. Chem. Phys* **1981**, *74*, 3190.
(35) Ishii, Y.; Terao, T.; Hayashi, S. *J. Chem. Phys.* **1997**, *107*, 2760.
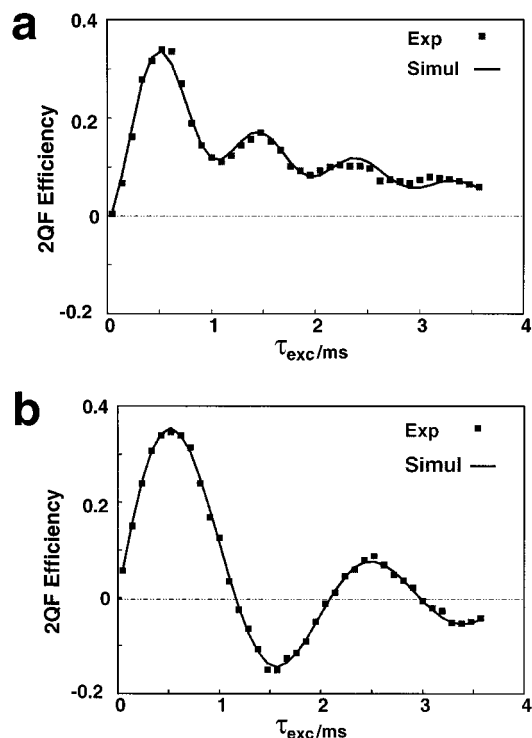(36) Lehmann, M. S.; Koetzle, T. F.; Hamilton, W. C. *J. Am. Chem. Soc* **1972**, *94*, 2657.

Figure 3. Experimental ^{13}C DQF efficiencies for [2,3-^{13}C$_2$]-L-alanine at 9.4 T and a spinning frequency $\omega_r/2\pi = 6.0$ kHz, together with the best fit simulations. The experiments were performed using R14$_2^6$ and a decoupling field equal to $|\omega_{nut}^H/2\pi| = 100$ kHz. (a) Symmetric procedure ($\tau_{exc} = \tau_{rec}$). (b) Asymmetric procedure ($\tau_{rec} = 523.8$ μs).

entire excitation cycles (at least in the procedures reported thus far), and this makes it difficult to digitize the rapid oscillations generated by short-range couplings. The maximum observed double-quantum filtering efficiencies in Figure 3 are around 35%. This is much less than the theoretical optimum, which is 73%.[2] We attribute the loss of signal to imperfect proton decoupling during the recoupling intervals.

2.3. CSA Compensation. The CSA dependences of three different pulse sequences are explored by numerical simulations in Figure 4. In a and b the simulated DQ build-up curves for POST-C7 and R14$_2^6$ are compared for a case with large CSA interactions ([10,11-^{13}C$_2$-all-E-retinal in a magnetic field $B^0 = 9.4$ T). The simulation parameters are summarized in Table 2. In each case, the plots show a superposition of 50 build-up curves for the symmetric procedure, simulated for an ensemble of CSA orientations, with the dipole−dipole coupling and CSA principal values held fixed. The Euler angles Ω_{PM}^j and Ω_{PM}^k relating the principal axis system of the CSA tensors to the molecular frame were varied independently (see refs 2, 3 for the notation). The Euler angles α_{PM}^j, α_{PM}^k, γ_{PM}^j and γ_{PM}^k were randomized in the range [0, 2π], while $\cos\beta_{PM}^j$ and $\cos\beta_{PM}^k$ were randomly distributed in the range [−1, 1]. Figure 4a shows the superposition of curves for R14$_2^6$, while Figure 4b shows the corresponding results for POST-C7. The higher scaling factor for R14$_2^6$ is visible. In addition, it may be seen that R14$_2^6$ is more robust than POST-C7 with respect to the CSA orientations. For example, the third maximum of R14$_2^6$ is spread over 200 μs, while the spread for POST-C7 is about 400 μs.

For comparison, Figure 4c shows simulated decay curves for the transverse magnetization under DRAWS, which is one of the most successful ^{13}C−^{13}C distance-measurement meth-

(37) Sun, B. Q.; Costa, P. R.; Kocisko, D.; Lansbury, R. T.; Griffin, R. G. *J. Chem. Phys.* **1995**, *102*, 702.

Solid-State NMR for Internuclear Distances

J. Am. Chem. Soc., Vol. 123, No. 43, 2001 10633
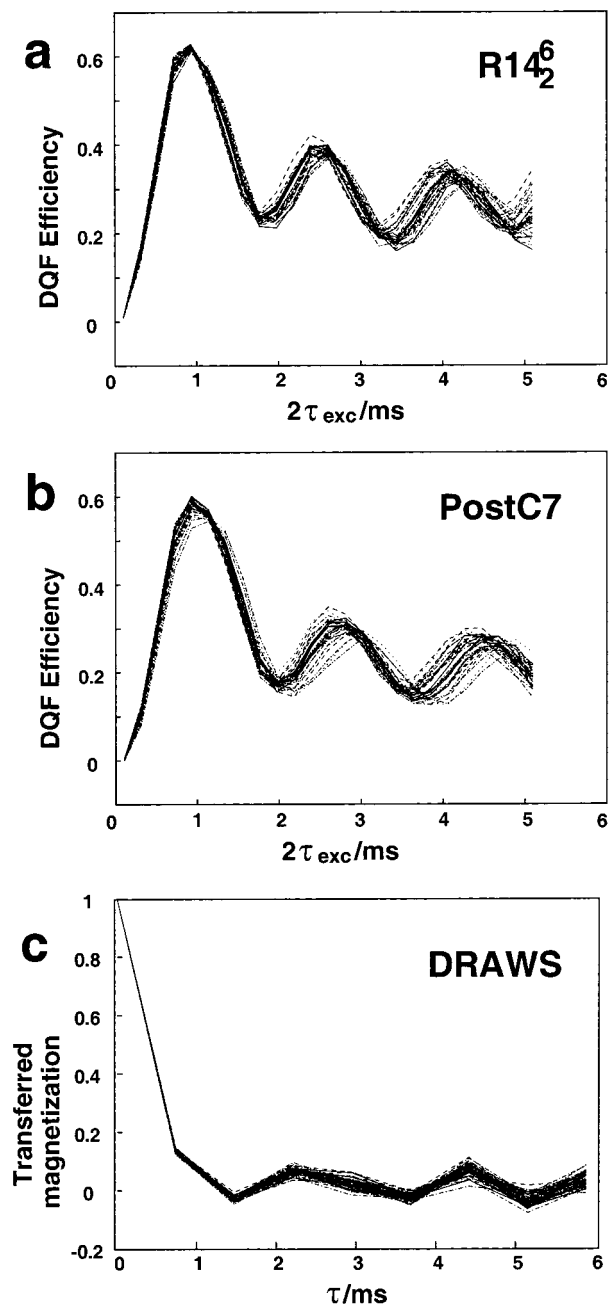
a

b

c

Figure 4. Simulations over an ensemble of 50 random CSA orientations using parameters corresponding to [11,12-$^{13}C_2$]-*all-E*-retinal (compound III) at 9.4 T and $\omega_r/2\pi = 5.5$ kHz. (a) DQ filtering efficiency using R14$_2^6$ (b) DQ filtering efficiency using POST-C7 (c) Trajectory of the transverse magnetization using DRAWS. In (a) and (b) a symmetric DQF procedure is used ($\tau_{exc} = \tau_{rec}$) with points acquired in steps of 104 μs using $\omega_{nut}^S/2\pi = 3.85$ kHz; in (c) the digitization step is determined by the supercycle duration and equals 727 μs with $\omega_{nut}^S/2\pi = 46.7$ kHz.

ods.[17,38,39] The simulations use the same spinning frequency as R14$_2^6$ and POST-C7. The digitization of the decay curve is poor (the digitization step is determined by the supercycle duration and equals 727 μs); the oscillations have small amplitude and are sensitive to the CSA orientations. In this case, the superiority of the R14$_2^6$ and POST-C7 methods is evident.

(38) Gregory, D. M.; Mehta, M. A.; Shiels, J. C.; Drobny, G. P. *J. Chem. Phys.* **1997**, *107*, 28.

(39) Kiihne, S.; Mehta, M. A.; Stringer, J. A.; Gregory, D. M.; Shiels, J. C.; Drobny, G. P. *J. Phys. Chem.* **1998**, *102*, 2274.

2.4. Supercycles. It is possible to improve the robustness of the sequences further by building phase-shifted supercycles. For example, the two-step supercycle

$$SRN_n^{\nu} = [RN_n^{\nu}]_0[RN_n^{\nu}]_{\pi} \tag{8}$$

where $[...]_{\phi}$ denotes an overall phase shift through the angle ϕ and has a reduced number of second-order terms in the average Hamiltonian $\bar{\mathscr{H}}^{(2)}$ according to the rule:

$$\bar{\mathscr{H}}^{(2)}_{l_2m_2\lambda_2\mu_2;l_1m_1\lambda_1\mu_1} = 0 \quad \text{if} \begin{cases} m_2n - \mu_2\nu \neq \frac{N}{2}Z_{\lambda_2} \\ \text{OR} \\ m_1n - \mu_1\nu \neq \frac{N}{2}Z_{\lambda_1} \end{cases}$$

$$\text{AND} \qquad \mu_2 + \mu_1 = Z_u \tag{9}$$

where Z_u is an odd integer. This rule applies in addition to the second-order selection rules described in refs 28, 29. For example, the symmetry R14$_2^6$ allows 20 CSA $\times$ CSA terms with $(l_2m_2\lambda_2\mu_2;l_1m_1\lambda_1\mu_1) = (2m_21\mu_2;2m_11\mu_1)$ and 16 CSA $\times$ DD cross-terms with $(l_2m_2\lambda_2\mu_2;l_1m_1\lambda_1\mu_1) = (2m_21\mu_2;2m_12\mu_1)$. For the supercycle SR14$_2^6$ the numbers of symmetry-allowed CSA $\times$ CSA terms and CSA $\times$ DD terms are reduced to 8 each.

Implementation of a supercycle does not require a sacrifice in the digitization of the build-up curve, since there is no requirement that integral supercycles are always completed. Other supercycle schemes have also been described,[4,7] but we have not implemented these yet in the context of $^{13}C-^{13}C$ distance measurements.

Supercycling is important when using long DQ excitation intervals, as in the case of medium-range distance measurements, but on a short time scale it is not essential.

2.5. Phase-Shift Tuning. An RN_n^{ν} sequence consists of $N/2$ repetitions of the element pair $R_{\phi_0}R'_{\phi_0}$, where the prime denotes sign reversal of phase shifts within the R elements and the phase shift ϕ_0 is exactly equal to $\pi\nu/N$. The sequence is well-behaved with respect to most common pulse imperfections, as discussed further below. However, the performance of the R sequences is very sensitive to the value of the phase ϕ_0. In some cases, a small adjustment of ϕ_0 by only a fraction of a degree has a major effect. This is illustrated in Figure 5, which shows experimental build-up curves for diammonium [2,3-$^{13}C_2$]-fumarate as a function of the phase shift ϕ_0, using the sequence R26$_8^9$ with $R = (\pi/2)_0(3\pi/2)_{\pi}$. As may be seen, the DQ filtering efficiency and the form of the curve are improved by an adjustment in the value of ϕ_0 by only 0.1° with respect to the theoretical value of 62.31°. The rather irregular dependence on ϕ_0 is probably due to the limited phase resolution of the 10-bit digital synthesizer (DDS) on this instrument. Clearly, phase resolution, accuracy, and stability are important issues for implementing these sequences.

The sensitivity of these sequences to the value of ϕ_0 may be understood by noting that the sequence $R_{\phi_0}R'_{-\phi_0}$ generates a rotation of the spins by $4\phi_0$ about the z-axis. The entire RN_n^{ν} sequence generates a spin rotation of $2N\phi_0$ about the z-axis. If ϕ_0 is exactly equal to $\pi\nu/N$, the complete rotation is through an angle of $2\pi\nu$, which is an integer multiple of 2π so that there is no net effect. However, any slight misset in the value of ϕ_0 accumulates over the sequence, causing phase shifts in the excited DQ coherence and a dramatic drop in efficiency. This is not the case for CN_n^{ν} sequences.

Table 2. Spin Interaction Parameters Used in the NMR Simulations for the Molecular Systems I−IX (Figure 8)

	I	II	III	IV	V	VI	VII	VIII	IX
$(j, k)^a$	(2,3)	(2,3)	(11,12)	(10,11)	(14,15)	(3,2)	(20,11)	(20,15)	(1,4)
$\delta_j^{iso} - \delta_k^{iso}$	0	0	−0.1	−3.7	−59.6	−31.0	−120.8	−176.3	0
δ_j^{aniso} (ppm)^b	94	87.9	−101.5	80.8	−70.0	−11.7	15.5	15.5	−64.8
$\eta_j{}^b$	0.59	0.80	0.78	0.98	0.99	0.76	1.0	1.0	0.82
$(\alpha_j, \beta_j, \gamma_j)^c$	(−65,−102,9)	(90,83,185)	unknown	unknown	unknown	(39,77,−53)	unknown	unknown	(16,97,−103)
δ_k^{aniso} (ppm)^b	94	87.9	81.7	−101.5	−92.5	−19.7	−101.5	−92.5	−64.8
$\eta_k{}^b$	0.59	0.8	0.93	0.77	0.51	0.44	0.77	0.51	0.82
$(\alpha_k, \beta_k, \gamma_k)^c$	(−65,−102,9)	(−90,97,185)	unknown	unknown	unknown	(82,24,29)	unknown	unknown	(16,97,−103)
$(\alpha_{jk}, \beta_{jk}, \gamma_{jk})^d$	(0,0,0)	(0,0,0)	(0,0,0)	(0,0,0)	(0,0,0)	(0,78,−35)	(0,0,0)	(0,0,0)	(0,0,0)
J_{jk} (Hz)^e	68	67	0	58.8	0	49	0	0	7
ref (NMR)^f	54	55	56	56	56	34, 57	56, 58	56, 58	54
$b_{jk}/2\pi$ (Hz)^g	−3350	−3238	−3166	−2530	−2453	−2151	−294	−275	−130

^{a} Assignment of ^{13}C spins to the molecular sites: site j is more shielded than site k. ^{b} CSA (deshielding units) and asymmetry parameter. ^{c} Euler angles (deg) relating the principal axis system of the CSA to the molecular reference frame. ^{d} Euler angles (deg) relating the principal axis system of the ^{13}C−^{13}C dipolar coupling to the molecular reference frame. ^{e} J couplings which are not known are assumed to be zero. Simulations verify that the DQ build up curves are very insensitive to the value of J_{jk}. ^{f} Reference to the NMR data. ^{g} Dipole−dipole coupling derived from the diffraction-estimated internuclear distances (see Table 3).
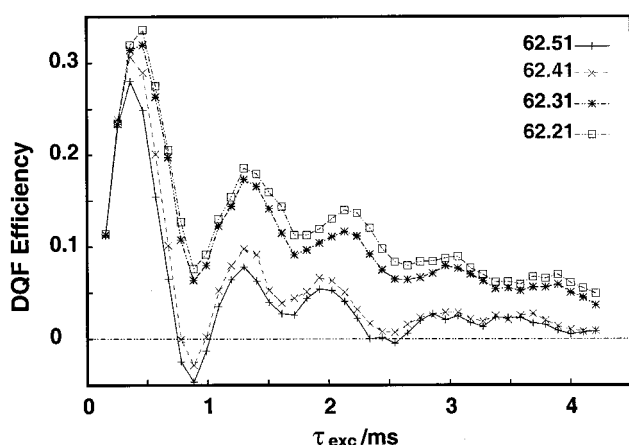

Figure 5. DQ build-up curves acquired at 4.7 T for diammonium [2,3-^{13}C$_2$]-fumarate using R26$_8^9$ and $\omega_r/2\pi = 11.850$ kHz, as a function of the phase ϕ_0 of the R elements. A symmetric procedure was used ($\tau_{exc} = \tau_{rec}$) with a decoupling field corresponding to $|\omega_{nut}^H/2\pi| = 100$ kHz. Note the extreme sensitivity to the value of the phase shift.

Simulations show that high-order cross terms associated with CSA interactions may also give rise to small z-rotations, which may be partly compensated by slight adjustments in ϕ_0. In the case of large CSA interactions, we improve DQ filtering efficiency by slightly adjusting the value of ϕ_0 away from the "theoretical value", sometimes by only a small fraction of a degree.

In practice, the phase ϕ_0 is adjusted individually for each sample by monitoring the amplitude of the DQ-filtered signal in the symmetric experiment for two cases: (i) in the region of τ_{exc} giving maximum DQ efficiency (typically close to 500 μs for directly bonded pairs), and (ii) around the next maximum, 1500 μs. The phase is varied in small steps close to the theoretical value $\pi\nu/N$, and the value maximizing both is chosen. Typically, the optimal phase shift is found to be within 0.5° of the theoretical value.

2.6. Radio-Frequency Transients. Ideal rf pulses are described by square waves with infinitesimal rise and fall time. In practice, there are transients at the leading and falling edge of pulses[40,41] and whenever a sudden phase shift is performed. This transient behavior is mainly due to the limited bandwidth of the tuned circuit in the probe and depends strongly upon the probe tuning. Since we require high accuracy for the distance

measurements, it is important to assess the effect of such transients on the DQ behavior.

There are four kinds of pulse transients: (i) in-phase symmetric and (ii) in-phase antisymmetric transients, with the transient having the same phase as the rf pulse; (iii) quadrature symmetric and (iv) quadrature antisymmetric transients, which are both 90°-phase-shifted with respect to the rf pulse. Symmetric transients have the same sign at the leading- and falling-edge of pulses; antisymmetric transients have the opposite sign. For a linear system, the transition at the junctions of pulses may be estimated by superposing the falling-edge transient of one pulse and the leading-edge transient of the subsequent one. Symmetric transients are not present in a linear system, and we have ignored them in the following discussion.

We have modeled the transient behavior of the current in the coil using a modified version of the electronic simulation program SPICE.[42] The predictions of this program are compared with experimental measurements of the rf transients in the coil, obtained by digitizing the signal generated in a small pick-up coil located near the sample and processing the accumulated data to derive the amplitude and phase of the rf signal as a function of time. The observations and simulations both agree with a simple model of the rf transients, in which the rf field in the coil at a time point t *just after* the junction of two pulses with the same amplitude and phases ϕ_1 and ϕ_2 has the following form:

$$\mathbf{B}_{rf}(t) = \mathbf{B}_{rf}^0(\phi_2) + \mathbf{B}_{rf}^{tran}(t, \phi_1) - \mathbf{B}_{rf}^{tran}(t, \phi_2) \quad t > t' \quad (10)$$

where the $\mathbf{B}_{rf}^0$ is the ideal field after the junction of the pulses:

$$\mathbf{B}_{rf}^0(\phi_2) = B_{rf}(\cos \phi_2 \, \boldsymbol{e_x} + \sin \phi_2 \, \boldsymbol{e_y}) \quad (11)$$

and the transient contributions have the following form:

$$\mathbf{B}_{rf}^{tran}(t, \phi) = \mathbf{B}_{rf}^{in-phase}(t, \phi) + \mathbf{B}_{rf}^{quad}(t, \phi) \quad (12)$$

with

$$\mathbf{B}_{rf}^{in-phase}(t, \phi) = B_{rf}\, e^{-\lambda_{tran}(t-t')}(\cos \phi \, \boldsymbol{e_x} + \sin \phi \, \boldsymbol{e_y}) \quad (13)$$

$$\mathbf{B}_{rf}^{quad}(t, \phi) = B_{rf}\, e^{-\lambda_{tran}(t-t')}\lambda_Q(t - t')(-\sin \phi \, \boldsymbol{e_x} + \cos \phi \, \boldsymbol{e_y}) \quad (14)$$

(40) Mehring, M.; Waugh, J. S. *Magn. Res.* **1972**, *43*, 649.

(41) Burum, D. P.; Linder, M.; Ernst, R. R. *J. Magn. Res.* **1981**, *43*, 463.

(42) Johnson, B.; Quarles, T.; Newton, A. R.; Pederson, D. O.; Sangiovanni-Vincentelli, A. *SPICE3*, 3rd ed.; Berkeley.
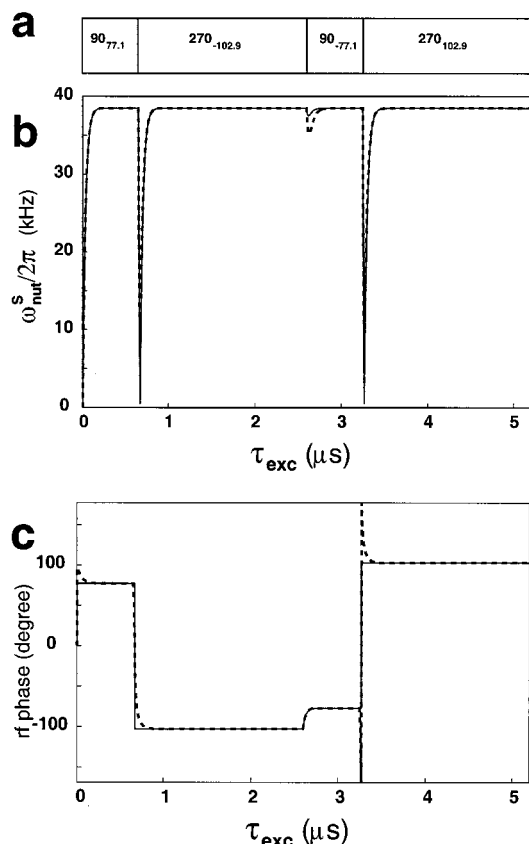
Figure 6. (a) First two elements of a $R14_2^6$ sequence. (b) Rf field amplitude in the coil for an exact match of the coil natural oscillation frequency and the rf frequency ($\lambda_Q = 0$, solid line) and for a tuning offset of 200 kHz ($\lambda_Q = 1.2 \times 10^6$ s^{-1}, dashed line). In all cases, the decay rate constant $\lambda_{\text{tran}} = 3.2 \times 10^6$ s^{-1} is used. (c) Phase of the rf field in the coil under the same conditions.

Here $\boldsymbol{e}_x$ and $\boldsymbol{e}_y$ are rotating frame axes, t' is the junction time-point, λ_{tran} is the transient decay rate constant, and λ_Q is the build-up rate constant of the quadrature transient.

In the probe used for the current experiments, the Q-value of the coil, as described in ref 43, is given by 200 at 100 MHz field, leading to a decay rate constant $\lambda_{\text{tran}} = 3.2 \times 10^6$ s^{-1}. The value of λ_Q depends strongly upon the difference between the natural oscillation frequency of the tuned circuit ω_{osc} and the rf driving frequency ω_{rf}. If the natural oscillation frequency is the same as the rf frequency, we get $\lambda_Q = 0$. In the case of a tuning offset of 200 kHz, electronic simulations indicate a value $\lambda_Q = 1.2 \times 10^6$ s^{-1}.

The amplitude and phase of the rf field in the coil during the first two R elements of the $R14_2^6$ sequence were calculated using eqs 10−14 and are shown in Figure 6(b) and (c). The solid lines show the case $\lambda_Q = 0$, that is, exact tuning. Note the strong amplitude transients at the edge of the 180° phase shifts and the smooth transition of the rf phase at the junction of the two R elements. When the coil is detuned by 200 kHz (dashed line), smooth phase transients are induced after the 180° phase shifts, while the rf amplitude is altered only slightly.

We have simulated the effect of these transients on the DQ build-up curves by incorporating the rf field shapes shown in Figure 6 into the accurate numerical simulations of the spin dynamics, using time steps of 20 ns in the rapidly changing regions. The simulation parameters correspond to diammonium [2,3-$^{13}C_2$]-fumarate in a field of 9.4 T (see Table 3). The

calculated asymmetric DQ build up curves are shown in Figure 7 for the following cases: ideal rectangular pulses, transients with $\lambda_Q = 0$ and transients with $\lambda_Q = 1.2 \times 10^6$ s^{-1}. Only a tiny variation in the oscillation frequency of the build-up curve is visible when the coil is detuned by 200 kHz. We conclude that this particular pulse sequence is well compensated for rf transients, in this low rf power regime.

3. Methods and Materials

3.1. Samples. A selection of $^{13}C_2$-labeled samples with a variety of $^{13}C-^{13}C$ distances and CSA parameters was used for evaluating these methods. The molecular structures of the labeled moieties are shown in Figure 8. The molecules are listed in order of increasing $^{13}C-^{13}C$ distance, as determined from X-ray or neutron diffraction data.

I. Diammonium [2,3-$^{13}C_2$]-fumarate. A 99%-$^{13}C_2$ sample was used. The $^{13}C-^{13}C$ distance determined by X-ray diffraction[44] is 131.4 pm.

II. Ammonium hydrogen[2,3-$^{13}C_2$]-maleate. A 99%-$^{13}C_2$ sample was used. The $^{13}C-^{13}C$ distance from X-ray diffraction[45] is 132.9 pm.

III. [11,12-$^{13}C_2$]-all-E-Retinal. The substance was synthesized by standard procedures[46] and recrystallized from *n*-pentane in the presence of 10-fold excess of unlabeled *all-E*-retinal. The $^{13}C-^{13}C$ distance determined by X-ray diffraction[47] is 133.9 pm. Note that the double bond is slightly lengthened by conjugation effects.

IV. [10,11-$^{13}C_2$]-all-E-Retinal. This was synthesized by standard procedures.[46] A 99%-$^{13}C_2$ sample was used. The $^{13}C-^{13}C$ distance determined by X-ray diffraction[47] is 144.3 pm. The single bond is slightly contracted by conjugation effects.

V. [14,15-$^{13}C_2$]-all-E-Retinal. This was synthesized by standard procedures[46] and recrystallized from *n*-pentane in the presence of 10-fold excess of unlabeled all-*E*-retinal. The $^{13}C-^{13}C$ distance determined by X-ray diffraction[47] is 145.8 pm. The single-bond is slightly shorter than standard due to conjugation.

VI. [2,3-$^{13}C_2$]-L-Alanine. This was obtained from Cambridge Isotope laboratories and used without any further purification or dilution. The bond length determined by X-ray diffraction is 152.3 pm.[36]

VII. [11,20-$^{13}C_2$]-all-E-Retinal. This was synthesized by standard procedures[46] and recrystallized from *n*-pentane in the presence of 10-fold excess of unlabeled *all-E*-retinal. The $^{13}C-^{13}C$ distance determined by X-ray diffraction[47] is 295.9 pm.

VIII. [15,20-$^{13}C_2$]-all-E-Retinal. This was synthesized by standard procedures[46] and recrystallized from *n*-pentane in the presence of 10-fold excess of unlabeled *all-E*-retinal. The $^{13}C-^{13}C$ distance determined by X-ray diffraction[47] is 302.4 pm.

IX. Diammonium [1,4-$^{13}C_2$]-fumarate. This was diluted to 6% with unlabeled material. The $^{13}C-^{13}C$ distance determined by X-ray diffraction[44] is 387.8 pm. In all cases, the principal values of the CSA tensors are known from previous measurements, and in some cases the orientations of the CSA principal axes are known too. We may therefore perform accurate simulations of the spin dynamics and also explore the influence of variable CSA orientations and pulse imperfection, such as rf inhomogeneity. Table 2 summarizes the spin interaction parameters for the $^{13}C_2$ pairs in these compounds.

3.2. Experimental. Most experiments were performed on a Varian Infinity 400 MHz spectrometer operating at a field of 9.4 T. In one case (Figure 5) a Varian Infinity 200 MHz spectrometer operating at a field of 4.7 T was used. The ^{1}H decoupling field corresponded to a nutation frequency of $\omega^I_{\text{nut}}/2\pi$ kHz during the R sequences (see Figure 2). Full 4 mm zirconia rotors were used (about 50 mg of material).

3.3. Simulations. All simulations were performed using the COM-PUTE algorithm, omitting relaxation, as described in refs 48, 49, 50. Powder averaging was done employing sets between 144 and 538 Euler

(43) Nilsson, J. W. *Electric Circuits*; Addison-Wesley: 1986.

(44) Hosomi, H.; Ito, Y.; Ohba, S. *Acta Crystallogr. C* **1998**, *54*, 142.
(45) Golic, L.; Leban, I. *Croatica Chem. Acta* **1982**, *55*, 41.
(46) Groesbeek, M.; Lugtenburg, J. *J. Photochem. Photobiol.* **1992**, *56*, 903.
(47) Hamanaka, T.; Mitsui, T. *Acta Crystallogr., Sect. B* **1972**, *28*, 214.
(48) Edén, M.; Lee, Y. K.; Levitt, M. H. *J. Magn. Res. A* **1996**, *120*, 56.
(49) Edén, M.; Levitt, M. H. *Mol. Phys.* **1998**, *95*, 879.
(50) Hohwy, M.; Bildsøe, H.; Jakobsen, H. J.; Nielsen, N. C. *J. Magn. Res.* **1999**, *136*, 6.

Table 3. Experimental Parameters, Simulation Conditions, and Distance Estimates

note	I	II	III	IV	V	VI	VII	VIII	IX
RN_n^ν	$R14_2^6$	$R14_2^6$	$R14_2^6$	$R14_2^6$	$R14_2^6$	$R14_2^6$	$SR22_4^9$	$SR22_4^9$	$SR22_4^9$
$\omega_r/2\pi$ (kHz)	5.5	5.5	5.5	5.5	5.5	6.0	7.0	7.0	7.0
τ_{rec} (μs)	364	363	363	468	442	623	3430	3430	6860
$\Delta\phi_0^a$	0	0	−0.2	−0.2	0	0	−0.3	−0.2	−0.3
$\Delta\omega_{nut}^S/\omega_{nut}^{S\ b}$	3	3	3	3	3	3	3	3	3
$(\Delta\alpha, \Delta\beta, \Delta\gamma)^c$	(20,0,20)	(0,0,0)	iso	iso	iso	(0,0,0)	iso	iso	(20,0,20)
N_{ens} ^{d}	100	100	400	400	400	100	400	400	100
a^e	0.6	0.9	0.8	0.8	0.6	0.7	0.8	0.5	0.7
$\{c_1, c_2\}$ $(s^{-1})^e$	{170,2200}	{380,4000}	{480,7000}	{330,3000}	{260,5000}	{225,3300}	{110,600}	{75,600}	{120,50}
$b_{jk}/2\pi$ (kHz)^f	−3127 ± 92	−3094 ± 56	−2917 ± 102	−2367 ± 78	−2388 ± 90	−2125 ± 38	−279 ± 7.5	−277 ± 17	−117 ± 28
r_{jk} (pm)^g	$134.5^{+1.3}_{-1.3}$	$134.9^{+0.8}_{-0.8}$	$137.6^{+1.7}_{-1.6}$	$147.6^{+1.7}_{-1.6}$	$147.1^{+1.9}_{-1.8}$	$152.9^{+1.0}_{-0.9}$	$301.1^{+2.7}_{-2.6}$	$301.8^{+6.6}_{-6.1}$	$401.6^{+38.7}_{-27.9}$
r_{jk} (pm) ^{h}	131.4	132.9	133.9	144.3	145.8	152.3	295.9	302.4	387.8

^{a} Phase adjustment of the pulses (in deg). The sequence is $R_{\phi_0}R'_{-\phi_0}$ with $\phi_0 = \pi\nu/N + \Delta\phi_0$. ^{b} rms deviation of rf field (%) used in the simulation ensemble. ^{c} rms deviation of Euler angles (in deg) used in the simulation ensemble. "iso" indicates an isotropic distribution $(\Delta\alpha, \Delta\beta, \Delta\gamma) = (360, 180, 360)$. ^{d} Number of simulations in the ensemble. ^{e} Average decay parameters for the biexponential function accounting for the DQ decay. ^{f} Determined value of the dipole−dipole coupling constant and its confidence limits, from this work. ^{g} Determined value of the internuclear distance and its confidence limits from this work, derived from b_{jk} neglecting motion and J anisotropy. ^{h} Diffraction estimates of the internuclear distance. See text for the sources.
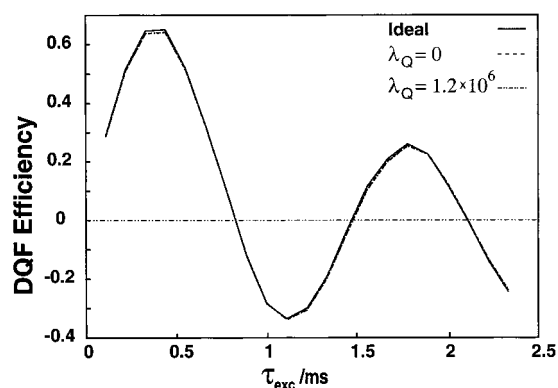

Figure 7. Effect of the rf transients on the DQ build up curves. The simulations correspond to column I in Table 2, at a field of 9.4 T. Solid curve: ideal rectangular pulses. Dashed line: including transients, with $\lambda_{tran} = 3.2 \times 10^6$ s^{-1} and $\lambda_Q = 0$. Dot−dashed line, $\lambda_{tran} = 3.2 \times 10^6$ s^{-1} and $\lambda_Q = 1.2 \times 10^6$ s^{-1}.

angles, specified by the Zaremba−Conroy−Wolfsberg scheme.[51] The simulated curves were multiplied by an empirical biexponential damping function of the form

$$ae^{-c_1 t} + (1 - a)e^{-c_2 t}, \quad 0 \leq a \leq 1, \quad c_1, \quad c_2 > 0 \quad (15)$$

where $t = \tau_{exc} + \tau_{rec}$, to obtain a best fit to the experimental results, taking into account efficiency losses related to low decoupling or other effects.

In principle, it should be possible to incorporate relaxation into the simulations in a more sophisticated way, by expressing the equation of motion in Liouville space.[52] However, such simultions would be far more time-consuming, involve a large number of adjustable parameters and still be of dubious validity since the damping of the coherences is dominated by heteronuclear interactions, which cannot be rigorously modeled by exponential damping. The biexponential damping model used here is purely empirical and is justified by the good match between the determined internuclear distances and the crystallographic data for the set of compounds examined in this paper.

4. Results

A series of DQ build-up curves were obtained at 9.4 T for compounds I−IX, using the experimental parameters given in the first three rows of Table 3. The observed DQ build up curves

(51) Conroy, H. *J. Chem. Phys.* **1967**, *47*, 5307.
(52) Helmle, M.; Lee, Y. K.; Verdegem, P. J. E.; Feng, X.; Karlsson, T.; Lugtenburg, J.; de Groot, H. J.; Levitt, M. H. *J. Magn. Res.* **1999**, *140*, 379.
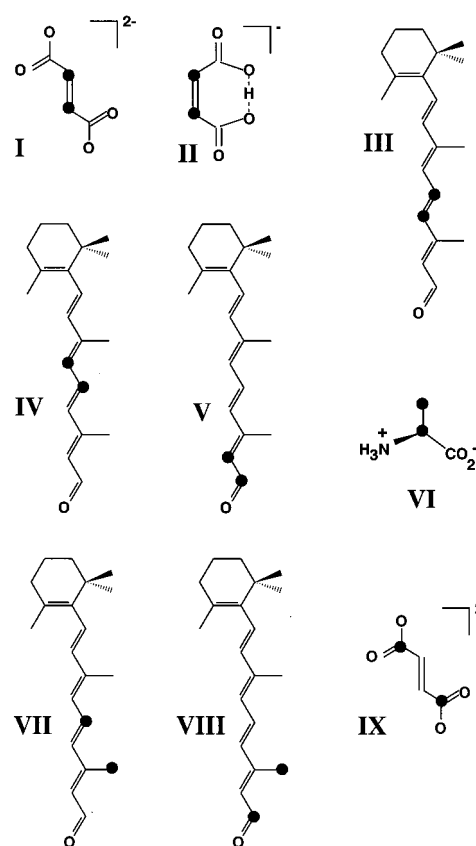

Figure 8. $^{13}C_2$-labeled species used in the distance measurement experiments.

were simulated numerically using the parameters in Table 2, with the exception of the dipole−dipole coupling, which was used as a fit parameter. Rf transients were ignored in these simulations. The experimental efficiencies were obtained by scaling the integrated DQ-filtered spectrum with respect to the integrated CP spectrum. The dipole−dipole coupling and damping rate constants were adjusted to find a global minimum in the mean square deviation. Experimental results and simulations are compared for two representative cases in Figure 9.

Although the biexponential damping model improves the quality of the fits, it has little effect on the estimated dipolar coupling, which is mainly determined by the frequency of the oscillations. The average biexponential fit parameters are listed in Table 3.
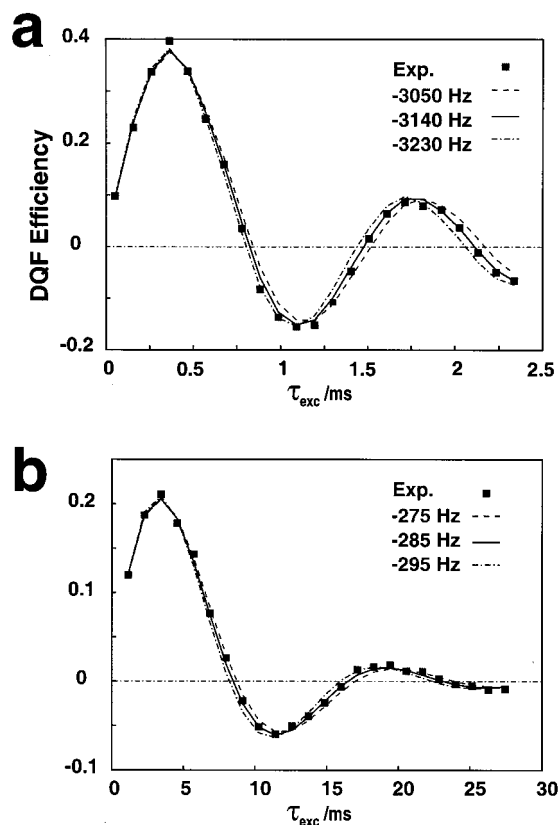
Figure 9. Experiments and simulations for two representative samples. The best fit simulation (solid line) is sandwiched between two additional simulations (dashed lines) corresponding to the error margins specified in Table 3. (a) Diammonium $[2,3\text{-}^{13}C_2]$-fumarate (compound I), (b) $[11,20\text{-}^{13}C_2]$-*all-E*-retinal (compound VII). For experimental parameters, see Table 3.

To assess the error limits on the estimate of the dipole−dipole coupling, we repeated the simulation over a large ensemble of input parameters, representing a distribution in the rf field amplitude and the uncertainty in the CSA tensor orientations. A Gaussian rf field distribution with standard deviation of 3% was assumed. This matches approximately the experimental rf field inhomogeneity in our probe. In addition, the Euler angles α, β, and γ specifying the CSA orientations were subjected to a normal distribution with an rms deviation specified in Table 3. The distributions of the fitted values of the dipole−dipole couplings were analyzed in order to obtain the confidence limits. The results are listed in Table 3.

If J anisotropy and the motional averaging[35] of the dipolar couplings are ignored, the measured dipole−dipole couplings may be converted into internuclear distance estimates by using eq 5. The estimated distance values of r_{jk} are compared with the literature data from diffraction experiments in Table 3.

Figure 10a summarizes these results for the six compounds containing directly bonded $^{13}C_2$ pairs. The bond lengths vary from around 130 pm for the double bond of $[2,3\text{-}^{13}C_2]$-fumarate (compound I) to around 153 pm for the single bond of $[2,3\text{-}^{13}C_2]$-L-alanine (compound VI). The solid-state NMR estimates are consistently slightly longer than the X-ray estimates. A statistical analysis of the six results shows that the distance overestimate is 2.7 pm with a standard deviation of 1.0 pm. This overestimate is presumably due to the neglect of molecular vibrational motion, J-coupling anisotropy, and rf transients. Motional modulation of the direction of the $^{13}C_2$ internuclear vector tends to reduce the dipole−dipole coupling and, hence, leads to a slight overestimate of the internuclear distance. The
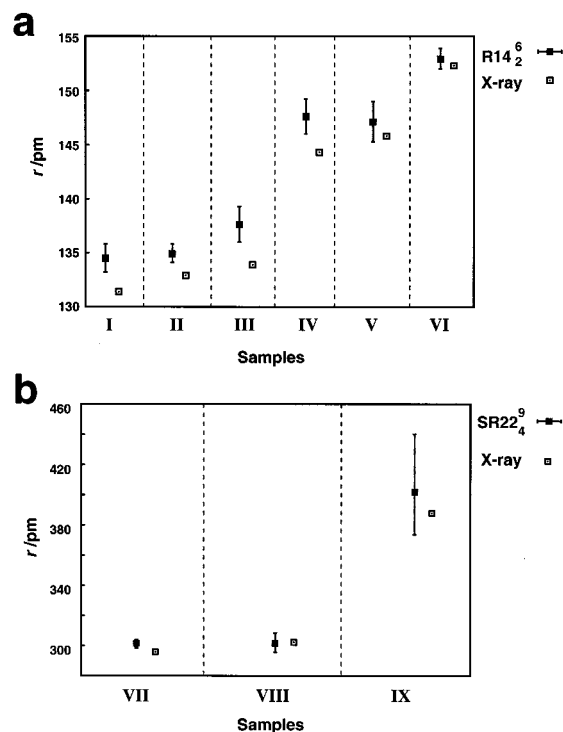

Figure 10. $^{13}C-^{13}C$ distance determinations at 9.4 T. The diffraction estimate of the internuclear distance is shown by a white square. The solid-state NMR estimate is shown by a filled square, with the indicated confidence limits. (a) Bond length measurements using $R14_2^6$, $R = (90)_0(270)_\pi$, $\omega_r/2\pi = 5.5$ kHz. (b) Medium-distance measurements with $SR22_4^9$, $R = (90)_0(270)_\pi$, $\omega_r/2\pi = 7.0$ kHz.

anisotropy in the J coupling may also contribute, although the few calculations of this quantity have concluded that it is of the order of the isotropic J coupling.[53] The J anisotropy is therefore too small to account completely for the discrepancy between the measured dipolar couplings and the X-ray distances, although it may be a contributing factor.

The confidence limits in the measured values of the dipole−dipole coupling are mainly determined by the uncertainties in the CSA orientations, expecially for the labeled retinals. These limits are consistently less that ±2 pm. Figure 10a shows that the method is easily capable of distinguishing between bonds of different order and is accurate enough to detect the lengthening of double bonds and shortening of single bonds in conjugated systems.

Figure 10b summarizes the distance estimates for the three compounds with medium-range distances in the range 300− 400 pm. The reported error limits derive from the confidence limits of the estimated dipolar couplings and are not symmetrical, due to the nonlinear relationship of these two quantities. As may be seen, the accuracy and precision for $[11,20\text{-}^{13}C_2]$-*all-E*-retinal (compound VII) and $[15,20\text{-}^{13}C_2]$-*all-E*-retinal (compound VIII) are very good. Note that no assumptions at all were made about the CSA orientations in these cases. The estimated distances are within 5 pm of the X-ray distances. In

(53) Kaski, J.; Lantto, P.; Vaara, J.; Jokisaari, J. *J. Phys. Chem.* **1998**, *120*, 3993.

(54) Bechmann, M.; Helluy, X.; Sebald, A. *J. Magn. Res.* **2001**. Submitted.

(55) Dusold, S.; Maisel, H.; Sebald, A. *J. Magn. Res.* **1999**, *141*, 78.

(56) Harbison, G. S.; Mulder, P. P.; Pardoen, H.; Lugtenburg, J.; Herzfeld, J.; Griffin, R. G. *J. Am. Chem. Soc.* **1985**, *17*, 4809.

(57) Nielsen, N. C.; Bildsøe, H.; Jakobsen, H. J.; Levitt, M. H. *J. Chem. Phys* **1994**, *101*, 1805.

(58) Verdegem, P. J. E.; Helmle, M.; Lugtenburg, J.; de Groot, H. J. M. *J. Am. Chem. Soc.* **1997**, *119*, 129.

the case of [1,4-^{13}C$_2$]-fumarate (compound IX), on the other hand, the confidence limits are very wide (about 30 pm). This is primarily because the oscillations in the build-up curve are barely visible at this rather long distance. The maximum DQ-filtering efficiency for compound IX was only 17%. The fitting of the curve is determined by the empirical damping function and the zero-crossing position. No attempt was made to analyze the relaxation behavior or correct for it, which is usually necessary for accurate long-range distance estimation.[13,16,17,38,39] More accurate long-distance estimates may probably be obtained by incorporating semiempirical relaxation parameters into the spin dynamics simulations, as in the case of rotational resonance.[13]

5. Conclusions

The results show that double-quantum solid-state NMR can provide accurate measurements of ^{13}C$-$^{13}C bond lengths and medium-range distances, even on compounds with fairly large chemical shift anisotropies. The precision of the method is around ±2 pm for internuclear distances up to 300 pm, with a systematic overestimate of the distance by 3 ± 1 pm, probably due to local molecular motion. For larger distances the accuracy and precision are degraded due to the slow damped oscillations of the DQ build-up curves. We expect this method to be potentially useful for investigating bonding changes in macro-molecules such as membrane proteins. Other applications, such as the study of surface-bound species, may also be envisaged. It is also possible to perform similar experiments at higher spinning frequency, using some of the other solutions listed in Table 1.

JA016027F